Optik - International Journal for Light and Electron Optics 227 (2021) 165969

Contents lists available at ScienceDirect

Optik

journal homepage: www.elsevier.com/locate/ijleo

Control the nanostructured growth of manganese oxide using starch: Electrical and optical analysis

H. Elhosiny Ali [a,d,f,*], M.M. Abdel-Aziz [a,c,*], A.M. Aboraia [b,g], I.S. Yahia [a,e,f], H. Algarni [a], V. Butova [b], Alexander V. Soldatov [b], Yasmin Khairy [d,**]

[a] Research Center for Advanced Materials Science (RCAMS), King Khalid University, Abha, 61413, P.O. Box 9004, Saudi Arabia
[b] The Smart Materials Research Institute, Southern Federal University, Sladkova 178/24, 344090, Rostov-on-Don, Russia
[c] Department of Physics, Faculty of Science, Al-Azhar University, Nasr City, Cairo, Egypt
[d] Physics Department, Faculty of Science, Zagazig University, 44519, Zagazig, Egypt
[e] Nanoscience Laboratory for Environmental and Biomedical Applications (NLEBA), Semiconductor Lab., Physics Department, Faculty of Education, Ain Shams University, Cairo, Egypt
[f] Advanced Functional Materials & Optoelectronic Laboratory (AFMOL), Department of Physics, Faculty of Science, King Khalid University, P.O. Box 9004, Abha, Saudi Arabia
[g] Department of Physics, Faculty of Science, Al-Azhar University, Assiut 71542, Egypt

ARTICLE INFO

Keywords:
Manganese oxide
Starch
X-ray diffraction
SEM
Diffused reflectance
Optical bandgap
Dielectric andelectrical characteristics

ABSTRACT

In this work, the influence of starch on the structure, and consequently, the properties of manganese oxide have been investigated at room temperature. Different weights of starch have been added to manganese nitrate during a solid-state combustion process. All the samples have been annealed at 600 °C for 2 h. The XRD (X-ray diffraction) and FT (Fourier transform)-Raman spectroscopy have shown the formation of α-Mn_2O_3 cubic structure for weight ratio equal to or less than (1/5) of starch/ $Mn(NO_3)_2$, while above this amount the phase changed to tetragonal phase Mn_3O_4. The crystallite size calculated via the Scherer equation is ranged from 21.3 nm to 23.8 nm. The strain and the dislocation density have values in the order of 10^{-3}. SEM (Scanning Electron Microscope) indicates a discrepancy in the size and the form of the particles due to the effect of starch weights. The sizes of spherical nanoparticles vary in the range of 780 nm - 30 nm. The energy gap estimated from the theory of Kubelka-Munk is reduced from 3.45 eV to 1.75 eV due to the effect of 0 and 0.5/5 ratio of starch/ $Mn(NO_3)_2$ and increased again to 2.63 eV for Mn_3O_4. Also, the dielectric permittivity has been influenced by starch weight. The electrical conductivity depends on the frequency and complies with the universal power law of Jonscher. Mn_3O_4 nanoparticles have been synthesized at low temperatures with a high percentage of low-cost starch with improved characteristics. Therefore, it is a promising material for the production of lithium manganese oxide to be employed in batteries of lithium.

1. Introduction

Nano-size materials are novel substances that are created rapidly and generally measured in one dimension, in dimensions from 1

* Corresponding authors at: Department of Physics, Faculty of Science, King Khalid University, P.O. Box 9004, Abha, Saudi Arabia.
** Corresponding author at: Physics Department, Faculty of Science, Zagazig University, 44519, Zagazig, Egypt.
E-mail addresses: hitham_ph@zu.edu.eg (H.E. Ali), msaleh2015.ma@gmail.com (M.M. Abdel-Aziz), yasmin_ph@zu.edu.eg (Y. Khairy).

https://doi.org/10.1016/j.ijleo.2020.165969
Received 22 April 2020; Received in revised form 13 June 2020; Accepted 3 November 2020
Available online 28 November 2020
0030-4026/

to 100 nm. The specific area rises rapidly at a nanometer-scale, with particle size decreasing, resulting in changes in the electromagnetic, mechanical, optical, and thermal characteristics of nanomaterials [1]. In numerous fields, the nanostructures are very suited to their applications. The most prominent instances of the contribution of nanotechnology in the energy industry are batteries and supercapacitors. Supercapacitors are classified as electrical double-level capacitors (EDLC) and pseudo-capacitors based on the charging storage system. The EDLC capacity results from the accumulation of charges at the electrode/electrolyte interface.

Moreover, it is utterly dependent on the electrode surface of the electrolyte. While with pseudo-capacitance, the transfer of charges from reversible faradic reactions is carried out on the electrode surface [2]. Electrodes are the main element in supercapacitors' development. Different transitional metal oxides, such as RuO_2 [3], Co_3O_4 [4], and manganese-based oxides [5], have been used as supercapacitors' electrode materials. Because of the high specific capacity, high power density, low cost, and environmentally friendly manganese oxide are promising electrode materials [6].

Combustion reaction for the synthesis of natural as well as blended oxide material is one of the supreme affordable, quick, and simple low energy mechanisms. The oxidation reaction thermally induced between oxidants (O, common anions of nitrate) and fuel (F, an organic molecule that kindles a reaction) supplies high surface and uniformly distributed oxide nanoparticles. Fuel's thermochemical characteristics and the F/O ratio also affect flame and all combustion mechanisms. Consequently, only the flame temperature parameter could be adjusted to regulate the crystalline particle phase, morphology, surface area, and other specific features of final oxide products [7].

It was reported that the starch molecule could be used as a green capping agent for producing the nanoparticles and the size control [8]. It takes helical conformation in the aqueous solution, where a wide number of −OH can expedite the metal ions complexation to the molecular matrix [9,10]. Thus, it offers stable surface protection or/and passivation to inhibit particle aggregation [11,12]. The starch was used previously to prepare spherical ZnO nanopowder in a diameter size range of 200−400 nm at 500 °C [13].

Manganese is a multi-oxidation transition metal that can provide several phases of manganese oxides such as MnO, MnO_2, Mn_2O_3, Mn_3O_4, and Mn_5O_8 [14]. The non-toxic, cheap, and plentiful manganese oxides are used in a wide variety of techniques, such as catalytic, electrochemical, optical, and electro-catalytic biosensors [15]. Manganese oxide is considered one of the most extensively explored transition metal oxides for various biomedical devices and acts as strong oxidants in biological systems, such as its ability to produce magnetic resonance contrast imaging [16]. However, owing to the strong property in quenching, they are always combined with fluorescent nanomaterials and explored as a sensor in biological devices [16]. Furthermore, it is a standard metal oxide materials for supercapacitor, Li-ion, and aqueous sodium-ion batteries, as well as for water treatment devices based on zero-valent metal and metal oxide nanomaterials [17–21]. MnO has a rock salt structure and can be considered the insertion of two FCC lattices. Manganese is present in higher oxidation levels - the prevalent manganese oxides are MnO_2, Mn_2O_3, and Mn_3O_4. The first one recognized as the hausmannite mineral at room temperature has a deformed spinal structure and the formula $Mn^{2+}\left[Mn_2^{3+}\right]O_4^{2-}$ [22] is displayed. Two polymorphs of Mn_2O_3 are also available, respectively, known as α-kurnakite and β-kurnakite/bixbyite minerals [14]. Mineral pyrolusite β-MnO_2, which is a simple tetragonal rutile structure, is the most stable and prevalent among manganese dioxides in nature [22]. The synthesis of manganese oxides has been explored to regulate the chemical composition, structure, size, and morphology of the nanoparticles because of their unique characteristics and broad applications [1]. Many conventional and efficient methods have served as a means to make nanomaterials with multiple shapes and outstanding characteristics for manganese oxides, such as hydrothermal [23], sol-gel synthesis [24], solid-state thermal decomposition [25], and pulsed laser deposition technique [26].

One of the essential phases of manganese oxide is manganese tetraoxide (Mn_3O_4), which is used as a catalyst for broadening series of reactions and a starting material in the creation of lithium manganese oxide that used in lithium batteries [27,28]. However, $Mn_3O_4$was obtained when MnO or Mn_2O_3 was heated in air to more than one thousand degrees [29]. A significant study was centered on fabricating Mn_3O_4 nano-crystalline and many productions that contain oxidation of Mn^{II} or decline of Mn^{VI} [30–32].

However, no much work has been done on the influence of starch concentration on the structure, shape, and size control of manganese oxide. Consequently, the current work aims to facile synthesized manganese oxide nanoparticles using a green capping agent such as starch, which served as a terminator for growing the particles. Moreover, we modified the nano-structural phase of the manganese oxide nanoparticles by varying the starch content. The phase, the structure, and the morphology of the samples were examined by XRD (X-ray diffraction), FT (Fourier transform)-Raman, and scanning electron microscope (SEM). The optical, electrical conductivity, and dielectric were also studied.

2. Experimental section

2.1. Mn_xO_y - nanoparticles synthesis

Combustion technique of solid-state synthesis was proceeded to produce nano-powder of manganese oxide; manganese nitrate and starch $(C_6H_{10}O_5)_n$ were used, respectively, as an oxidant and a fuel in the combustion. The procedure of synthetic is based on the oxidation reaction. 0, 0.001, 0.01, 0.1, 0.25, 0.5, 1, and 10 g of starch was reacted to 5 g of $Mn(NO_3)_2$. After that, each weight of starch is grinded with manganese nitrate and all of them are placed on a hot plate for one day at 60 °C. secondly, the resulting mixtures were evaporated to dryness at 80 °C for two hours before forming foam at 600 °C after three hours to expel carbon in the form of CO_2 resulting from the combustion of nitrate - starch mixture. The samples have been marked MCH1 (pure $Mn(NO_3)_2$), MCH2 (0.001/5 ratio of starch/ $Mn(NO_3)_2$), MCH3 (0.01/5 ratio of starch/ $Mn(NO_3)_2$), MCH4 (0.1/5 ratio of starch/ $Mn(NO_3)_2$), MCH5 (0.25/5 ratio of starch/ $Mn(NO_3)_2$), MCH6 (0.5/5 ratio of starch/ $Mn(NO_3)_2$), MCH7 (1/5 ratio starch/ $Mn(NO_3)_2$), and MCH8 (10/5 ratio of starch/ $Mn(NO_3)_2$).

2.2. Reaction mechanism

Starch comes from various sources of botanical, containing potatoes, corn, and wheat. However, all granules contain two main components of molecular, amylopectin and amylose; both of them are polymers of a-glucose units in the $^4C_1$ conformation. In the amylose has connected (1 → 4), with the oxygen ring atoms and all on the same side, while in amylopectin about one residue in every twenty is also linked (1 → 6) creating branch-points. The starch utilized in this work made up the amylose molecular form (Aldrich S9765, Soluble, ACS reagent). Starch is water-soluble when the temperature of a cloudy solution reaches 75 °C, and the semi-crystalline structure is lost. When we added the solution of $Mn(NO_3)_2$ to the starch solution, the oxygen in the OH branch attracted the metal cations. Upon a heating process, the amount of water is reduced, the smaller molecules of amylose start forming a network that holds water, and raises the mixture's viscosity. This procedure is a so-called gelatinization of starch. The nitrate decomposed to nitrogen dioxide and oxygen upon the process of heating and will be removed from the compounds.

2.3. Mn_xO_y - nanoparticles characterization

Crystal structure of the synthesized Mn_xO_y – nanoparticles have been identified by powder X-ray diffraction using prototypical Shimadzu XRD – 6000 diffractometers with CuK_α radiation (1.5418 $\AA$) at 40 kV in the range of 10° to 80° with a step of 0.02° of 2θ and one second for each step. For calculating the lattice parameters, the retviled refinement was used. The morphology of Mn_xO_y-nanoparticles has been verified using the Scanning Electron Microscope (SEM; JSM-6360) model with a 10-kV operating voltage. Using the thermo-scientific DXR Raman Microscope Installation Excitation [532 nm Laser Type Diode-Pumped, Solid State (DPSS)], the vertical (V) polarized FT(Fourier transform) - Raman spectra of the prepared samples were gained and the time of acquisition was set at 30 s. The laser output is set at ten mW. The incoming signal on the vertical surface of the nanoparticle sample and the V-polarized Raman scattered signal was gathered in a backscattering geometry with a 100x microscope objective.

To study the optical properties for all powder samples, a diff ;used reflectance measurement was carried out using Shimadzu 3600 with integrating sphere attachment. Dielectric and ac conductivity were investigated using a 4200-SCS KEITHLEY semiconductor device at room temperature with applied frequency oscillating from 3 kHz to 10 MHz using a uniquely designed holder. The electrical properties were documented by fixing the samples inside a holder with two brass electrodes. The lowest electrode was made as a bottom contact of the samples, while the higher electrode is linked to spring for good contact with the upper part of the tested sample without any external pressure on both electrodes. The superior electrode has a diameter of 0.01 m. An isolated material of Teflon was used to separate the upper and lower contacts. The experiment was prepared as in the next consequence: First lowest electrode, the sample under test, higher electrode, and lastly, Teflon bar linked between the two electrodes.

3. Results and discussion

3.1. Structure characterization of α-Mn_2O_3 and Mn_3O_4 nanoparticles

3.1.1. XRD patterns

X-ray diffraction patterns for all Mn_xO_y nanoparticles synthesized by starch assisted combustion method are shown in Fig. 1. Phase identification was performed by comparing the structural parameters detected with the standard patterns of diffraction. Fig. 1 demonstrates XRD patterns with and without starch added to $Mn(NO_3)_2$. The intense crystalline peaks observed for the pristine Mn $(NO_3)_2$ [MCH1] XRD spectrum observed at Bragg's angles 23.20°, 33.08°, 38.32°, 45.28°, 49.42°, 55.32°, and 65.94°. These crystalline peaks attributed to the planes (211), (222), (400), (332), (431), (440) and (622), respectively, corresponded to the standard patterns (JCPDS reference card # 00 – 041 – 1442) corresponding to the typical cubic bixbyite Mn_2O_3 ($a = c$ =9.409 Å), with the space group Ia – 3 (206). Furthermore, no other phases of manganese oxide are present, which shows the high purity of the phase of the prepared

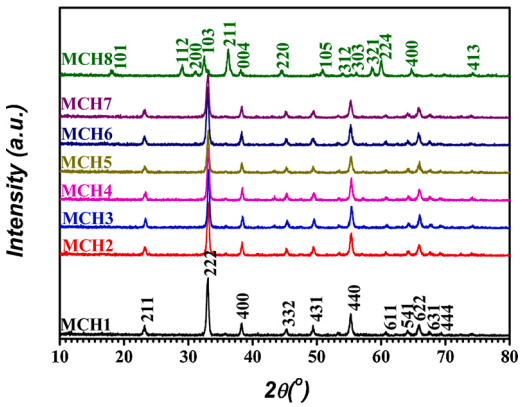

Fig. 1. XRD patterns of Mn_xO_y NPs with different ratios of starch to $Mn(NO_3)_2$.

Mn_2O_3 sample. The line broadening of the X-Ray shows that the synthesized sample has a nanocrystalline nature. The peaks of Mn_xO_y NPS following the addition of starch by ratios range (0.001/5 – 1/5) and almost no changes were found, as shown in Fig. 1. The diffraction peaks of the different planes correspond to the cubic Mn_2O_3 bixbyite structure. These results confirmed the presence of Mn_2O_3 in Mn_xO_y starch nanocomposites. The absence of starch diffraction peaks due to the complete decomposition of starch. Upon increasing the starch ratio to 10/5 (MCH8), the broad diffraction peaks assigned to tetragonal (a =5.7650 Å, c =9.4420 Å) hausmannite Mn_3O_4 phase (JCPDS No. 01 – 080 – 0382) will result, with 141/am (141) space group. The results suggest that the addition of large amounts of starch deforms the crystal lattice and causes the oxygen defect of the solid-state interface reaction, resulting in the formation of the spinel structure of Mn_3O_4 instead of Mn_2O_3 [33].

The effect of starch quantity on the phase of manganese oxide could be attributed to the reduction properties of this organic compound. In more detail, the chemical process of $Mn(NO_3)_2$ decomposition is presented in Scheme 1. The formation of oxygen leads to the oxidation of manganese ions from Mn^{2+} (in nitrate salt) to Mn^{3+} (in Mn_2O_3 oxide). Starch plays the role of the fuel in the combustion process and decomposes to carbon dioxide and water (Scheme 2). Thus, for the samples MCH1-MCH7, the only reactions are (1) and (2). However, when the amount of starch is the highest (MCH8 sample), its oxidation is not complete. Some byproducts could be formed, such as carbon, carbon monoxide, and others. Therefore, the most probable reaction scheme, which results in the formation of carbon admixture, was reported in Scheme 3. Formed carbon could interact with oxygen (from reaction 1) and reduce Mn_2O_3 oxide with the formation of Mn_3O_4 form with a mixed oxidation state of manganese - +2/+3 (Scheme 4).

(1) $2Mn(NO_3)_2 \xrightarrow{600^{\circ}C} Mn_2O_3 + 4NO_2 + 0.5O_2$

(2) $[C_6H_{10}O_5]_n + 6nO_2 \xrightarrow{600\,^{\circ}C} 6nCO_2 + 5nH_2O$

(3) $[C_6H_{10}O_5]_n + 6n - xO_2 \xrightarrow{600\,^{\circ}C} 2xC + 6n - xCO_2 + 5nH_2O$

(4) $3Mn_2O_3 + 0.5C \xrightarrow{600\,^{\circ}C} 2Mn_3O_4 + 0.5CO_2$

The lattice parameters for the synthesized samples have calculated using the relationship

$$a = d_{(hkl)}\sqrt{h^2 + k^2 + l^2} \tag{1}$$

where a is the lattice parameter, $d_{(}$hkl$)$ is the interplanar spacing, and (hkl) are the Miller indices. Mn_xO_y sample undoped and starch doped lattice parameters are estimated using the corresponding formula and are described systematically in Table 1. Variation of the lattice constants between 9.410 $\AA$ and 9.408 $\AA$ when the starch ratio changes from 0 to 1/5, shows that the grain samples are strained and may alter owing to the characteristics and concentrations of the natural imperfections. The high strain in the lattice caused by raising the content of starch to 10 g influences the redistribution of the cations from the cubic site to the tetrahedral site, according to the XRD study.

The mean crystallite size and strain of the synthesized samples were determined using Scherrer's formula:

$$D = k\lambda/\beta cos\theta \tag{2}$$

$$\varepsilon = \beta/4tan\theta \tag{3}$$

where D, ε, k, λ, β and θ are the average particle size, strain due to crystal imperfections and distortion, the shape function ($k = 0.9$), the full width at half maximum intensity (FWHM) and the Bragg's angle, respectively. The average particle size and the strain are signified in Table 1. The average particle size calculated for the MCH1 sample was ~21.38 nm, whereas the particle size increased to ~23.82 nm, with the increase in starch concentration to 0.1 g. This increase may be due to starch-caused forced aggregation. The average particle size of Mn_2O_3–starch composites were estimated to be ~ 22.71 nm, and thus for Mn_3O_4 (MCH8 sample) is ~21.87 nm, as shown in Table 1.

Dislocations are a crystal imperfection associated with the misregistration of the lattice in one portion of the crystal concerning another portion. Dislocations, unlike vacancies or interstitial atoms, are not equilibrium imperfections, i.e., thermodynamic considerations are not enough for their existence in the observed densities [34]. The density of dislocation is determined using the formula [22]:

$$\delta = 1/D^2 \tag{4}$$

The variation of dislocation density with starch concentration is shown in Table 1. It can be noticed that there is an increase in the number of lattice imperfections in the samples and a decrease in the size of the crystallite, which is attributed to the reduction in the grain boundary with the increase of the starch content up to 0.1 g. This can be attributed to the improvement of crystallinity because atoms are arranged regularly in the crystal lattice. Furthermore, the particle size decreases, while the density of dislocation and the

$$2Mn(NO_3)_2 \xrightarrow{600\,^{\circ}C} Mn_2O_3 + 4NO_2 + 0.5O_2$$

Scheme 1. The oxidation of manganese ions from Mn^{2+} (in nitrate salt) to Mn^{3+} (in Mn_2O_3 oxide).

$$[C_6H_{10}O_5]_n + 6nO_2 \xrightarrow{600\,^{\circ}C} 6nCO_2 + 5nH_2O$$

Scheme 2. The role of Starch in the combustion process.

$$[C_6H_{10}O_5]_n + 6n\text{-}xO_2 \xrightarrow{600\,^{\circ}C} 2xC + 6n\text{-}xCO_2 + 5nH_2O$$

Scheme 3. The most probable reaction scheme and the production of carbon admixture.

$$3Mn_2O_3 + 0.5C \xrightarrow{600\,^{\circ}C} 2Mn_3O_4 + 0.5CO_2$$

Scheme 4. The formation of Mn_3O_4 with a mixed oxidation state of manganese - +2/+3.

Table 1
XRD Parameters and the estimated energy gap of the synthesized α-Mn_2O_3 and Mn_3O_4 Nanomaterials.

Samples	The crystallite size, (nm)	Lattice strain, (10^{-3})	Dislocation density, (10^{-3} nm^{-2})	Space group	a, (Å)	c, (Å)	E_{g1}, (eV)	E_{g2}, (eV)
MCH1	21.4	1.84	2.19	Ia-3	9.409	9.409	3.45	–
MCH2	23.2	4.28	1.85	Ia-3	9.409	9.409	2.31	1.75
MCH3	23.4	3.99	1.83	Ia-3	9.408	9.408	2.15	1.69
MCH4	23.8	3.99	1.76	Ia-3	9.410	9.410	2.51	1.55
MCH5	22.1	4.52	2.05	Ia-3	9.409	9.409	1.75	1.64
MCH6	21.8	4.45	2.11	Ia-3	9.408	9.408	1.82	1.58
MCH7	21.9	4.37	2.07	Ia-3	9.408	9.408	1.84	1.63
MCH8	21.9	5.21	2.09	I41/amd	5.765	9.442	2.63	–

micro-strain increased. The lower value of dislocation density means that the use of starch in the synthesis of Mn_2O_3 and Mn_3O_4 NPs increases the crystallinity of nanomaterials.

3.1.2. Raman spectra

To gather information on structural defects like lattice disorders or oxygen vacancies, Raman spectroscopy is a successful technique [35]. In this context, we used this method to study the impact of starch on the structure of the samples. Fig. 2 indicates the room temperature of the Raman spectra for nanoparticles Mn_2O_3 and Mn_3O_4. The peaks positioned at 307−366 cm^{-1}, 642−658 cm^{-1}, and 476 cm^{-1} are ascribed, respectively, to the modes of stretching of each Mn_xO_y products [36]. The peak at around 642 cm^{-1} is typical of the Raman spectrum of Mn_2O_3 products confirming the unique nanostructure of space-group *Ia–3*. This peak strength is corresponding to the extending vibrations of the bridged oxygen species, and it was moved to a higher wavenumber of ~658 cm^{-1} by increasing the starch content to 1 g (MCH7), accompanied by the increase in the peak intensity. This effect indicates that, due to the influence of starch, the symmetric stretch of the Mn_2O_3 group changes.

Furthermore, other bands were formed and continuously grown at approximately 366 cm^{-1} and 476 cm^{-1} by increasing the starch content to 0.1 g (MCH4) and 0.25 g (MCH5), respectively. These peaks have a relatively low intensity, which could be attributable to the scattering of phonons produced by smaller grains and specific development defects, such as vacancy clusters, oxygen vacancy, and

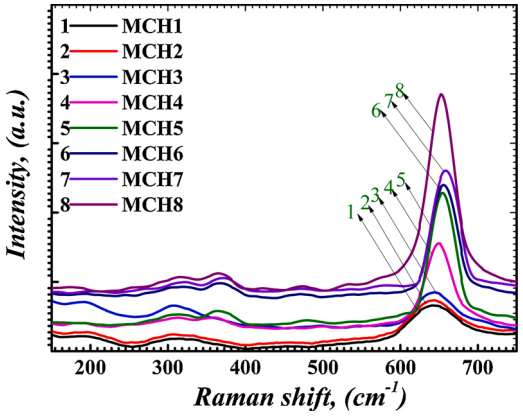

Fig. 2. Raman spectra of Mn_xO_x NPs with different ratios of starch.

local lattice disorder on the interface and surface of the Mn_2O_3 nanoparticles. However, the broad peaks at small wavenumber regions are of weak intensities and correspond to the deformation modes of the Mn—OM—n metal-oxygen chain.

Moreover, under the same conditions, the band at ~652 cm^{-1} was formed with the increment of the starch contents up to 10 g (MCH8). This peak was observed in different previous work for various Mn_xO_y, and it is close to that of Mn_3O_4 bulk (~655 cm^{-1}) [37, 38] and probably ascribed to an Mn–O–Mn stretch in the sample. Another mode with an extremely low intensity was observed in the

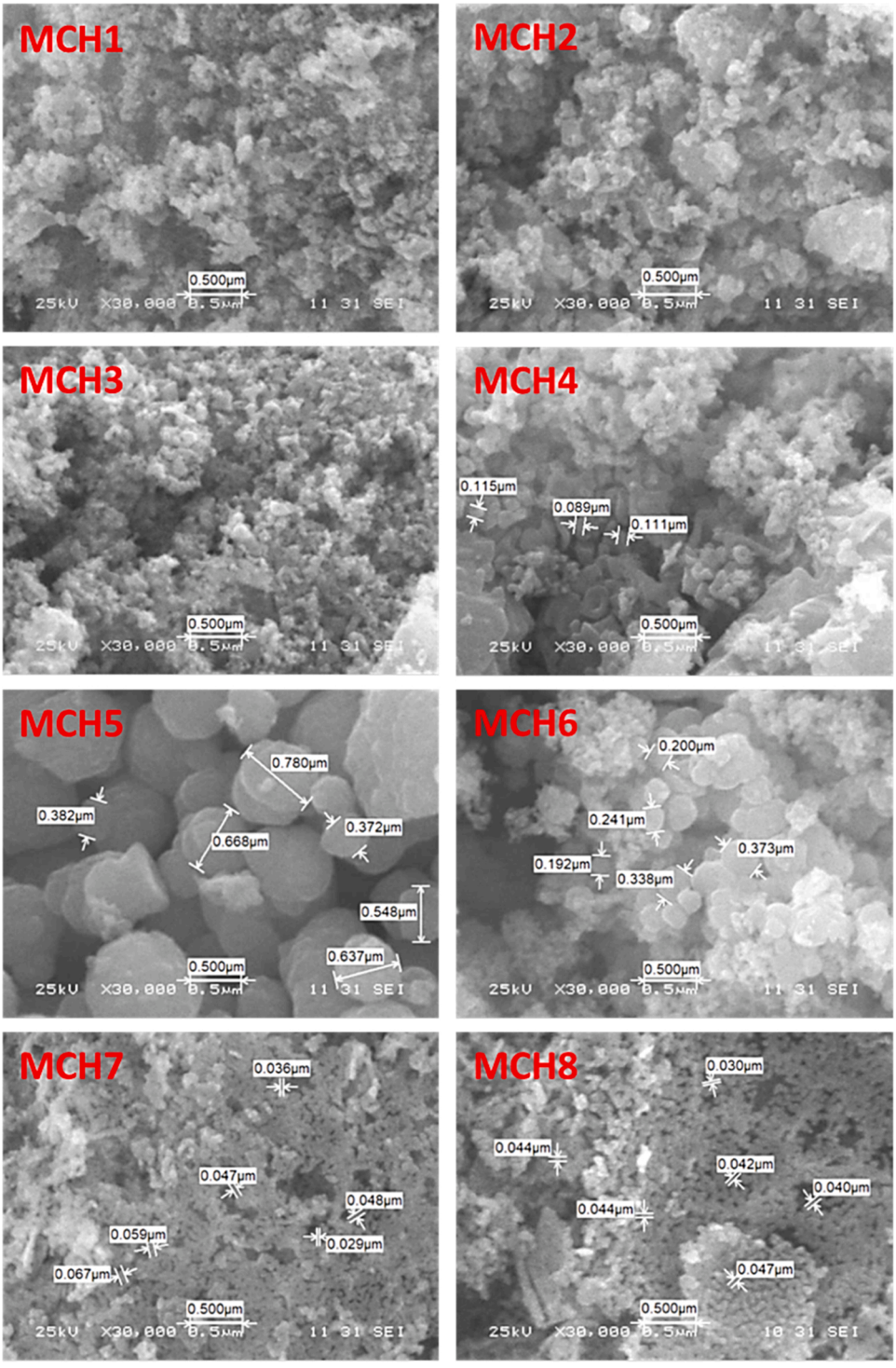

Fig. 3. SEM micrographs of Mn_xO_y NPs with various percentages of starch at high magnification.

MCH8 sample at 531 cm^{-1}, which is attributed to bridge oxygen species asymmetric stretching. Therefore, the Mn_3O_4 group only is generated when the content of starch is higher than 10 g. Nevertheless, the spectra of Raman in Fig. 2 shows the structural transformation of Mn_2O_3 to Mn_3O_4, which is observed in the MCH8 sample with a starch content of 10 g. This is probably due to the loss of lattice oxygen, which leads to the reconstruction of the phase. These results are confirmed by the XRD analysis that shows the change of structure from Mn_2O_3 to Mn_3O_4 samples by increasing the starch percentage, where the oxygen diffusion may generate the reverse phase transformation from bulk to the surface.

3.2. Morphology characterization

The morphology of the synthesized Mn_xO_x nanoparticles at different ratios of starch has been examined by the SEM analysis and shown in Fig. 3. The morphology of the samples changed with the concentration of starch. Due to the existence of the Van der Waals force, the agglomerations took place during the synthesis process [39]. The MCH1, MCH2, and MCH3 have not specific shape, whereas with increasing the starch ratio, a spherical shape was generated. MCH4 image shows different shapes of particles. On the other hand, at high content of starch (0.25 g), i.e., MCH5 sample, the morphological transformation into nanosheets was performed with a size range of 372 nm–780 nm, which attributed to the removal at the nucleation stage of relatively unstable particles [40]. It is possible to observe a different morphology of particles of variable sizes (192–373) nm for MCH6. This could be attributed to feathers with agglomeration and aggregation of particles [39]. As the weight of starch $\geq$ 1 g, the architectures tended to be flakes-like nanostructure of size (30–67) nm range with a large number of pores, as shown in Fig. 3. Therefore, it indicates that the starch ratio plays a key character in the formation of nanoparticles and their shape as well as nanoporous. The presence of porous nature in Mn_xO_x makes the adsorption characteristic easier, indicating an excellent adsorbent to use as an appropriate catalyst for the application of Mn_xO_x [39].

3.3. Optical characterization

One of the methods used to measure the absorption and scattering of light from a powder sample is the diffused reflectance (DR). The optical analysis of the synthesized samples was performed in the range between 200 and 2500 nm. Fig. 4 displays the DR for Mn_xO_y nanoparticles at ratios of starch (from 0 to 10/5).

It is obvious from Fig. 4 that there is an absorption edge of the specimens shifted to a higher wavelength, which suggests the reduction of the bandgap. However, the absorption edge of MCH6 and MCH8 samples shifted towards the lower wavelength. The Kubelka-Munk function (*F(R)*) was measured as a function in the reflectance (*R*) by the relation [41]:

$$F(R) = (1-R)^2/2R \tag{5}$$

Moreover, the linear absorption coefficient can be related to the Kubelka-Munk function (*F(R)*) by the relation [41]:

$$\alpha = F(R)/t \tag{6}$$

where *t* is the powder thickness in the designed holder. The absorption band gap E_g of the Mn_xO_y nanoparticles can be obtained using Tauc's equation:

$$\alpha = \frac{B}{h\upsilon}\left(h\upsilon - E_g\right)^x \tag{7}$$

where α is the absorption coefficient, It is characterized by the energy consumed in the medium in unit length and proportional with the quantity *F(R)*. Moreover, *B* is a constant that depends on the probability of transition, $h\nu$ is the photon energy, E_g is the optical band gap, and *x* is an exponent that specifies the type of electronic transitions that might occur during the photon absorption process [42]. For direct transition $x = ½$, while for indirect transition $x = 2$.

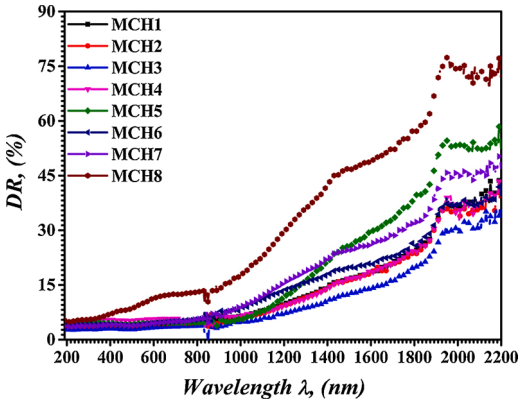

Fig. 4. DR spectra of Mn_xO_y NPs with various ratios of starch.

The absorption coefficient associated with the electronic transition from the valance band to the conductive band can be used to determine the value of the optical band gap E_g for nanoparticles [39]. Fig. 5 indicates the absorption factor in the form of $(F(R)h\upsilon/t)^2$ as a function of the photon energy $(E = h\upsilon)$ for the as-synthesized samples. To determine the bandgap at different starch concentrations of the as-synthesized Mn_xO_y nanoparticles, the intercepts of the straight lines with the photon energy axis are characterized. The estimated energy gap is listed in Table 1 for all as-synthesized Mn_xO_y nanoparticles with different starch content. The optical band gap for pure Mn_2O_3 nanoparticles [MCH1 sample] was found to be 3.45 eV, and for Mn_xO_y nanoparticles synthesized with starch content ratios from 0.001/5 to 10/5 of $Mn(NO_3)_2$ [MCH2 – MCH5] samples were found to be decreased from 2.44 eV to 1.75 eV. Moreover, the forbidden optical gap increased to 1.82 eV and 2.63 eV for the MCH6 and MCH8 samples (Mn_3O_4 NPS). The direct optical E_g values are in good agreement with previous Mn_xO_y nanoparticles reports [43,44]. Such values indicate that the nanoparticles of manganese oxide are semiconductors. The broad optical energy gap values of the as-synthesized Mn_xO_y NPs were reported in a range of extremely efficient photovoltaic materials. Synthetic samples could, therefore, be considered as potential materials in solar cell applications for the processing of solar radiation [45]. Variations in the bandgap values could be attributed to the structural order-disorder at the lattice site by the introduction of starch, thereby changing the energy levels within the material bandgap.

3.4. Electrical characterization

3.4.1. Dielectric studies

The real and imaginary components of dielectric constant characteristics of the Mn_xO_y NPs were evaluated in the 3 kHz – 10 MHz frequency region for the sample with different starch levels from 0 to 10/5 of $Mn(NO_3)_2$. The real dielectric frequency-dependent ε' was determined using the formula [46]:

$$\varepsilon' = \frac{C_p t}{\varepsilon_o A} \tag{8}$$

where C_p is the capacitance of the specimen in farad, t is the specimen thickness (0.5 mm), ε_o is free space permittivity (8.85×10^{-12} F/m), and A is the specimen cross-sectional area [46]. The real part of dielectric constants versus different frequencies is shown in Fig. 6. It is found that with increasing frequency, the dielectric constant decreases and increased again at a higher frequency for all synthesized samples. The reduction of dielectric constants shows that good conductive grains are formed surrounded by poorly conductive (isolating) grain boundaries [47]. The higher values of the dielectric at lower frequencies can be interpreted by the influence of space charge polarization. With the introduction of external electrical fields, the space charge moves and is trapped with defects in the sample interfaces. This causes a polarization inside the synthetic samples, which can be induced and observed by the high value of the real dielectric constant near the region of low-frequency. As a consequence of charge trapping, the grain boundaries are electrically efficient, where grains at higher frequency ranges are active. Moreover, at high frequencies, the real dielectric constant is nearly increased, which can be attributed to the reduction in polarization with increasing frequency. This can be because of the fast change in the electric field beyond the high frequency of an external electrical field, which in turn causes electronic polarization [47].

For the dielectric loss of the present solid systems, it is possible to observe a similar manner, as seen in Fig. 7. The dielectric loss (ε'') of the solid system can be calculated from the next relation:

$$\varepsilon'' = \varepsilon' * tan\delta \tag{9}$$

where $tan\delta$ is the measured loss tangent. The high values of the ε'' at low- frequency can be related to the movement of free ions within the samples. With raising the frequency, the dielectric loss decreased gradually and increased again at a higher frequency owing to the vibration of the molecules inside the systems.

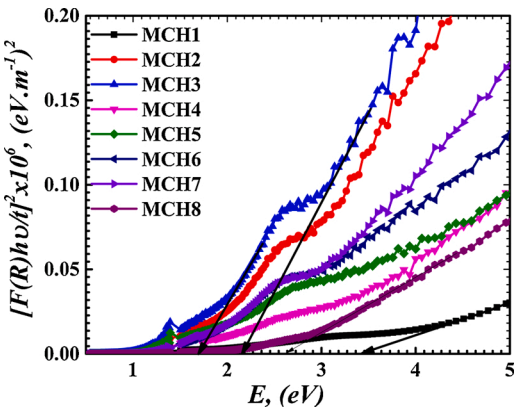

Fig. 5. Tauc's plot, $(F(R)h\upsilon/t)^2$ versus the photon energy $(h\upsilon)$ for Mn_xO_y NPs with various percentages of starch.

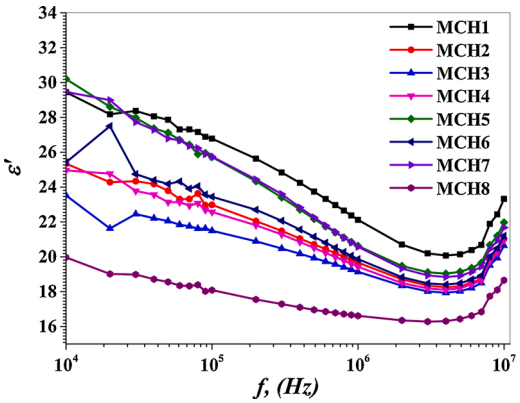

Fig. 6. Variation of the real part of dielectric constant with *f (Hz)* for all samples.

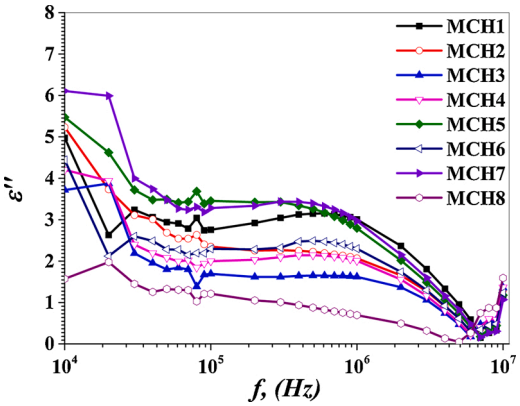

Fig. 7. Variation of dielectric loss ($\varepsilon^{''}$) with frequency for all samples.

3.4.2. AC electrical conductivity studies

Electrical conduction is the capability of a material to perform an electrical current. Thus, the response of AC electrical conductivity was considered to obtain more information about the electrical properties and the responsibility for the conduction process of the investigated samples. The following relationship can measure the AC electrical conductivity of the Mn_xO_y NPs:

$$\sigma_{total.\,ac}(\omega) = \frac{t}{ZA} \tag{10}$$

$$\sigma_{total.ac}(\omega) = \sigma_{ac}(\omega) + \sigma_{dc}(\omega = 0) \tag{11}$$

$$\sigma_{ac}(\omega) = \sigma_{total.ac}(\omega) - \sigma_{dc}(\omega = 0), \tag{12}$$

$$\sigma_{ac}(\omega) = A\omega^{s}, \tag{13}$$

where Z is the impedance. The angular frequency ω related to the ac conductivity σ_{ac} *(2πf)* by the empirical universal law of Jonscher (*Eq.* (11)), in which s is a fractional exponent frequency.

Fig. 8 displays the change of ac conductivity σ_{ac} with Mn_xO_y NPs frequency. The behavior of ac conductivity σ_{ac} has been found to increase with an increasing frequency for all samples. The electron hopping model can be used to describe the electrical conduction process [48]. In the region as their conductivity increases significantly as a result of electronic hopping, there is no increase in the number of charge carriers. The inset of Fig. 8 shows the frequency exponent (s), which was estimated from the data fitting, versus the weight of starch in gram. It is clear, from the inset of Fig. 8, that the slope of the plots (s) > 1, which could be linked to the electronic conduction mechanism. A similar result was reported [49].

4. Conclusion

A combustion technique was successfully developed to synthesize Mn_3O_4 with uniform nano-sizes at low temperatures by increasing the starch content ratio to 10/5 of $Mn(NO_3)_2$. All synthesized samples were calcined at 600 °C/2 h after drying. The XRD

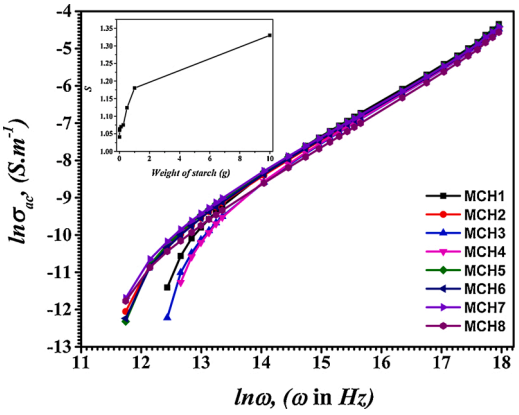

Fig. 8. Variation of ac conductivity with frequency for all samples.

patterns and Raman study for all samples revealed the development of the α-Mn_2O_3 cubic bixbyite due to the starch weight ratio effects from 0.001/5 to 1/5 of $Mn(NO_3)_2$ while increasing the amount of starch to 10 g the tetragonal Mn_3O_4 is initiated with crystallite size from Scherer equation of 21.87 nm. Using the SEM technique, the Mn_3O_4 has a uniform nano-grain size of approximately 160 nm. Its bandgap is estimated via Kubelka-Munk theory and found to be 2.63 eV. The values of dielectric permittivity ($\varepsilon_r^{'}$) for all samples vary from 19 to 32 with the influence of starch content and decrease with increasing frequency. The ac-conductivity also depends on the frequency and follows the empirical universal law of Jonscher. The homogeneous Mn_3O_4 nanoparticles formation at low temperature, due to the effect of a large amount of starch (10 g), with a low bandgap makes them appropriate for lithium-ion batteries and ferrites (manganese zinc) fabrications.

Authors statement

1 The work described in the present article has not been published previously.
2 It is not under consideration/submitted for publication elsewhere.
3 Its publication is approved by all authors and tacitly or explicitly by the responsible authorities where the work was carried out.
4 That, if accepted, it will not be published elsewhere including electronically in the same form, in English or in any other language, without the written consent of the copyright-holder.
5 The work described in the present article has not been published previously.
6 All authors have checked the manuscript and have agreed to the submission.

Declaration of Competing Interest

The authors report no declarations of interest.

Acknowledgments

The authors extend their appreciation to the Research Center for Advanced Materials Science (RCAMS), King Khalid University for funding this work under grant number RCAMS/KKU/015-20.

References

[1] S. Sagadevan, J. Mater. Sci. Eng. 04 (03) (2015), https://doi.org/10.4172/2169-0022.1000172.
[2] B. Gnana Sundara Raj, A.M. Asiri, J.J. Wu, S. Anandan, J. Alloys Compd. 636 (2015) 234–240, https://doi.org/10.1016/j.jallcom.2015.02.164.
[3] T. Audichon, T.W. Napporn, C. Canaff, C. Morais, C. Comminges, K.B. Kokoh, J. Phys. Chem. C 120 (5) (2016) 2562–2573, https://doi.org/10.1021/acs.jpcc.5b11868.
[4] H. Chen, J. Wang, F. Liao, X. Han, Y. Zhang, C. Xu, L. Gao, Ceram. Int. 45 (9) (2019) 11876–11882, https://doi.org/10.1016/j.ceramint.2019.03.070.
[5] N. Kumar, K. Guru Prasad, A. Sen, T. Maiyalagan, Appl. Surf. Sci. 449 (2018) 492–499, https://doi.org/10.1016/j.apsusc.2018.01.025.
[6] R. Aswathy, M. Ulaganathan, P. Ragupathy, J. Alloys Compd. 767 (2018) 141–150, https://doi.org/10.1016/j.jallcom.2018.07.067.
[7] D. Visinescu, B. Jurca, A. Ianculescu, O. Carp, Polyhedron 30 (17) (2011) 2824–2831, https://doi.org/10.1016/j.poly.2011.08.006.
[8] K. Vidhya, M. Saravanan, G. Bhoopathi, V.P. Devarajan, S. Subanya, Appl. Nanosci 5 (2015) 235–243.
[9] Q. Wei, S.H. Kang, J. Mu, Colloids Surf. A Physicochem. Eng. Asp. 247 (2004) 125–127.
[10] P.R. Babu, K. O'Connor, R. Seeram, Prog. Biomater. 2 (8) (2013) 1–16.
[11] P. Raveendran, J. Fua, L. Scott, Green Chem. 8 (2006) 34–38.
[12] C. Engelbrekt, K.H. Sorensen, J. Zhang, A.C. Welinder, P.S. Jensen, J. Ulstrup, J. Mater. Chem. 19 (2009) 7839–7847.
[13] G. Zhang, X. Shen, Y. Yang, J. Mater. Chem. Phys. C 115 (2011) 7145–7152.
[14] M. Sharrouf, R. Awad, M. Roumié, S. Marhaba, Mater. Sci. Appl. 06 (10) (2015) 850–859, https://doi.org/10.4236/msa.2015.610087.
[15] R.R. Muthuchudarkodi, C. Vedhi, Appl. Nanosci. 5 (4) (2015) 481–491, https://doi.org/10.1007/s13204-014-0340-3.
[16] Md Nurunnabi, Jason McCarthy (Eds.), Biomedical Applications of Graphene and 2D Nanomaterials, Elsevier, 2019.

[17] S. Mohapatra, T.A. Nguyen, P. Nguyen-Tri (Eds.), Noble Metal-Metal Oxide Hybrid Nanoparticles: Fundamentals and Applications, Elsevier, 2018.
[18] R. do Nascimento, O.P. Ferreira, A.J. De Paula, V.D.O.S. Neto, Nanomaterials Applications for Environmental Matrices: Water, Soil and Air, Elsevier, 2019.
[19] Y. Wang, J. Liu, B. Lee, R. Qiao, Z. Yang, S. Xu, X. Yu, L. Gu, Y.S. Hu, W. Yang, K. Kang, Nat. Commun. 6 (1) (2015) 1–10.
[20] C. Liu, C. Zhang, H. Song, C. Zhang, Y. Liu, X. Nan, G. Cao, Nano Energy 22 (2016) 290–300.
[21] Chun Zhan, T. Wu, J. Lu, K. Amine, Energy Environ. Sci. 11 (2018) 243–257.
[22] R. Tholkappiyan, A.N. Naveen, K. Vishista, F. Hamed, J. Taibah Univ. Sci. 12 (5) (2018) 669–677, https://doi.org/10.1080/16583655.2018.1497440.
[23] H.S. Roy, M.Y.A. Mollah, M.M. Islam, M.A.B.H. Susan, Polym. Bull. 75 (12) (2018) 5629–5643, https://doi.org/10.1007/s00289-018-2355-5.
[24] F.E. Sarac, U. Unal, Electrochim. Acta 178 (2015) 199–208, https://doi.org/10.1016/j.electacta.2015.07.169.
[25] J.W. Long, J.M. Wallace, G.W. Peterson, K. Huynh, ACS Appl. Mater. Interfaces 8 (2) (2016) 1184–1193, https://doi.org/10.1021/acsami.5b09508.
[26] A.D. Khalaji, F. Malekan, J. Cluster Sci. 25 (2) (2014) 517–521, https://doi.org/10.1007/s10876-013-0631-y.
[27] M. Fehse, R. Trócoli, E. Hernández, E. Ventosa, A. Sepúlveda, A. Morata, A. Tarancón, Thin Solid Films 648 (2018) 108–112, https://doi.org/10.1016/j.tsf.2018.01.015.
[28] E.R. Stobhe, A.D. de Boer, J.W. Geus, Catal. Today 47 (1999) 161–167.
[29] Process for preparing lithium manganese oxides, U.S Patent number: 6706443,(2004), Horst Krampitz, Gerhard Wohner.
[30] N.N. Greenwood, A. Earnshaw, Chemistry of the Elements, 2nd ed., Butterworth-Heinemann, 1997. ISBN 978-0-08-037941-037948.
[31] Hausmannite Mn3O4 nanorods: synthesis, characterization and magnetic properties Jin Du et al, Nanotechnology 17 (2006) 4923–4928.
[32] A. Vázquez-Olmos, R. Redón, G. Rodríguez-Gattorno, M.E. Mata-Zamora, F. Morales-Leal, A.L. Fernández-Osorio, J.M. Saniger, J. Coll. Interface Sci. 291 (2005) 175–180.
[33] X. Sun, J. Liu, Y. Li, Chem. Eur. J. 12 (7) (2005) 2039–2047.
[34] R. Manigandan, K. Giribabu, S. Munusamy, S. Praveen Kumar, S. Muthamizh, T. Dhanasekaran, A. Padmanaban, R. Suresh, A. Stephen, V. Narayanan, CrystEngComm 17 (14) (2015) 2886–2895, https://doi.org/10.1039/C4CE02390K.
[35] M. Bedir, A. Tunç, M. Öztas, Acta Phys. Pol. A 129 (6) (2016) 1159–1164, https://doi.org/10.12693/APhysPolA.129.1159.
[36] X. Yang, X. Yu, M. Lin, X. Ma, M. Ge, Catal. Today 327 (2019) 254–261, https://doi.org/10.1016/j.cattod.2018.04.041.
[37] Y.-F. Han, F. Chen, Z.-Y. Zhong, K. Ramesh, E. Widjaja, L.-W. Chen, Catal. Commun. 7 (10) (2006) 739–744, https://doi.org/10.1016/j.catcom.2006.08.006.
[38] T. Larbi, K. Doll, T. Manoubi, J. Alloys Compd. 688 (2016) 692–698, https://doi.org/10.1016/j.jallcom.2016.07.041.
[39] B.J. Rani, M. Ravina, G. Ravi, S. Ravichandran, V. Ganesh, R. Yuvakkumar, Surf. Interfaces 11 (2018) 28–36, https://doi.org/10.1016/j.surfin.2018.02.007.
[40] A. Vijayamari, K. Sadayandi, S. Sagadevan, P. Singh, J. Mater. Sci. Mater. Electron. 28 (3) (2017) 2739–2746, https://doi.org/10.1007/s10854-016-5853-y.
[41] D.P.M.D. Shaik, R. Pitcheri, Y. Qiu, O.M. Hussain, Ceram. Int. 45 (2, Part A) (2019) 2226–2233, https://doi.org/10.1016/j.ceramint.2018.10.135.
[42] H. Elhosiny Ali, Y. Khairy, Optik 178 (2019) 90–96, https://doi.org/10.1016/j.ijleo.2018.10.049.
[43] Y. Khairy, M.M. Abdel-Aziz, H. Algarni, A.M. Alshehri, I.S. Yahia, H.E. Ali, Mater. Res. Express 6 (11) (2019), 115346, https://doi.org/10.1088/2053-1591/ab4e34.
[44] B.K. Pandey, A.K. Shahi, R. Gopal, Mater. Focus. 2 (3) (2013) 221–226, https://doi.org/10.1166/mat.2013.1078.
[45] M. Karimi, M.J. Eshraghi, J. Alloys Compd. 696 (2017) 171–176, https://doi.org/10.1016/j.jallcom.2016.11.259.
[46] H. Elhosiny Ali, Y. Khairy, H. Algarni, H.I. Elsaeedy, A.M. Alshehri, I.S. Yahia, J. Mater. Sci: Mater. Electron. 29 (2018) 20424.
[47] M.M. Abdel-Aziz, H. Algarni, A.M. Alshehri, I.S. Yahia, H. Elhosiny Ali, Mater. Res. Express 6 (12) (2019), 125321, https://doi.org/10.1088/2053-1591/ab56d8.
[48] M. Mehedi Hassan, W. Khan, A. Azam, A.H. Naqvi, J. Ind. Eng. Chem. 21 (2015) 283–291, https://doi.org/10.1016/j.jiec.2014.01.047.
[49] A.N. Papathanassiou, I. Sakellis, J. Grammatikakis, Appl. Phys. Lett. 91 (2007) 122911.